



High-performance for hydrogen evolution and pollutant degradation of reduced graphene oxide/two-phase g-C₃N₄ heterojunction photocatalysts

Chengjie Song^{1,2} · Mingshan Fan¹ · Weidong Shi¹ · Wei Wang²

Received: 29 September 2017 / Accepted: 6 February 2018 / Published online: 10 March 2018
© Springer-Verlag GmbH Germany, part of Springer Nature 2018

Abstract

We have successfully synthesized the composites of two-phase g-C₃N₄ heterojunction photocatalysts by one-step method. And the reduced graphene oxide/two-phase g-C₃N₄ heterojunction photocatalyst was fabricated via a facile hydrothermal reduction method. The characterization results indicated that the two-phase g-C₃N₄ was integrated closely, and the common phenomenon of agglomeration for g-C₃N₄ was significantly reduced. Moreover, the oxidized graphene was reduced successfully in the composites and the graphene was overlaid on the surface or the interlayers of g-C₃N₄ heterojunction composite uniformly. In addition, we have carried out the photocatalytic activity experiments by H₂ evolution and rhodamine B removal, tetracycline removal under the visible light irradiation. The results revealed that the composite has improved the separation efficiency a lot than the pure photocatalyst. The photocurrent test demonstrated that the recombination of electrons and holes were efficiently inhibited as well as enhanced the photocatalytic activity. The 0.4% rGO loaded samples, 0.4% rGO/CN₂, own the best performance. Its rate of H₂ evolution was 15 times as high as that of the pure g-C₃N₄.

Keywords Homojunction g-C₃N₄ · Photocatalysis · Hydrothermal reduction method

Introduction

Photocatalytic decomposition of water is a most advanced method to solve the global energy and environmental problems (Liu et al. 2017; Walter et al. 2010; Xu et al. 2016a; Xu et al. 2017a). Over the past couple of decades, immense amounts of metal-oxide, oxynitride, and sulfide semiconductor photocatalysts have been developed for efficient photocatalytic water splitting to the H₂ and photocatalytic degradation

of pollutants to the non-toxic small-molecule compounds (Hou et al. 2014; Hu et al. 2015; Wu et al. 2016; Yan et al. 2015). However, these catalysts mostly contain the toxic heavy metals to limit their development extremely. Thus, the metal-free photocatalyst was expected to research.

Recently, the metal-free polymeric graphitic carbon nitride (g-C₃N₄) has attracted much attention to investigate its ability for water splitting and environmental purification under visible-light irradiation (Cao & Yu 2014; Shi et al. 2014; Xu et al. 2014). The g-C₃N₄ photocatalysts, with a two-dimensional (2D) nanosheet structure, possess appropriate band gap, large surface area, and excellent thermal and chemical stabilities, which made it become a very potential material for photocatalytic applications (Dong et al. 2013b; Venditti et al. 2015; Zhang et al. 2014). Unfortunately, there is a common drawback of high electron-hole recombination rates in the semiconductor materials. To form a heterojunction with other semiconductor photocatalysts is one of the effective strategies to resolve this problem. Many researches have been

Responsible editor: Suresh Pillai

✉ Weidong Shi
swd1978@ujls.edu.cn

¹ School of Chemistry and Chemical Engineering, Jiangsu University, Zhenjiang 212013, People's Republic of China

² School of Municipal and Environmental Engineering, Harbin Institute of Technology, Harbin 150000, People's Republic of China

successfully investigated to enhance the photocatalytic activities of g-C₃N₄ by the fabrication of heterojunctions, which mainly focused on many complexes of metal-based semiconductors and g-C₃N₄, for example, InVO₄/g-C₃N₄, TiO₂/g-C₃N₄, Cu₂O/g-C₃N₄, MoS₂/g-C₃N₄, TaON/g-C₃N₄, CdS/g-C₃N₄, and NaNbO₃/g-C₃N₄ (Chen et al. 2014; Hu et al. 2015; Huang et al. 2013; Hurum et al. 2003; Liau et al. 2013; Song et al. 2015; Sun et al. 2003; Sun et al. 2012; Wang et al. 2013; Wang et al. 2012; Yan et al. 2010; Zhao et al. 2015). Very recently, the studies showed that g-C₃N₄ with different band gap structure could be synthesized by different precursors, such as urea, thiourea, melamine, cyanamide, triazine, and more carbon- and nitrogen-containing compounds (Hong et al. 2012; Wu et al. 2016; Xu et al. 2013; Xu et al. 2016b; Xu et al. 2017b; Yuan et al. 2018). A few metal-free photocatalytic heterojunctions from different phases of g-C₃N₄ had been fabricated. Dong et al. reported that the junctions of two-phase g-C₃N₄ from thiourea and urea can show the very high charge-separation rate and the excellent photocatalytic activity for NO removal under visible light irradiation (Dong et al. 2013b). Shalom et al. had synthesized a highly efficient two-phase g-C₃N₄ junction photocatalyst from the supramolecular complexes of cyanuric acid, melamine, and barbituric acid for the hydrogen production (Shalom et al. 2014; Yuan et al. 2014). In addition, as an excellent electron transporter, graphene that contained the two-dimensional network of Sp²-bonded carbon atoms has been well used to improve the activity of single-phase g-C₃N₄ photocatalysts (Shown et al. 2014; Su et al. 2012; Xiang et al. 2012). Xiang et al. synthesized the graphene/g-C₃N₄ with the high photocatalytic activities for H₂ production (Shown et al. 2014). The result indicates that the graphene can act as an electronic conductive channel to efficiently transfer the interfacial photogenerated charge carriers and enhance the photocatalytic activities of g-C₃N₄. However, to the best of our knowledge, no studies on the fabrication and photocatalytic activities of graphene/two-phase g-C₃N₄ heterojunction photocatalysts have been reported until now.

Herein, the reduced graphene oxide/two-phase g-C₃N₄ heterojunction photocatalyst was fabricated via a facile hydrothermal reduction method. The photocatalysts were characterized by XRD, FE-SEM, TEM, FTIR, XPS, PL, UV-Vis DRS, and electron spin resonance (ESR). The hydrogen evolution, RhB removal, and TC removal were used to evaluate the activity of the as-prepared samples. The ratio of precursor also has been researched.

Experimental section

All chemical reagents in this work were of analytical grade and were used without further purification.

Preparation of photocatalysts

The urea and melamine were dried at 60 °C for 2 days to make them dry completely, and all of the samples were synthesized by thermal treatment. Firstly, urea and melamine were taken place in alumina crucibles after grinding evenly with a reasonable mass ratio in Table 1. The precursors were heated to 550 °C at a heating rate of 2.3 °C min⁻¹ in a muffle furnace and maintained for 4 h.

The graphene oxide (GO), AR grade, was purchased from Aladdin. Reduced graphene oxide/CN2 (CNM or CNU) samples were synthesized by hydrothermal reduction method. In a typical synthesis, 0.1 g CN2 was added to the solution, which containing 40 mL distilled water and 20 mL ethyl alcohol, and the solution was stirred. The weight ratios of GO to CN2 were 0.2, 0.4, and 0.6%, and the corresponding samples were named as 0.2% rGOCN2, 0.4% rGOCN2, and 0.6% rGOCN2, respectively. After ultrasonication for 2 h, the mixture solution was transferred into a 100 mL of Teflon-lined stainless-steel autoclave and was heated at 120 °C for 6 h. Finally, the obtained products were washed several times with distilled water and absolute ethanol and dried at 70 °C for 12 h after the autoclave was cooled to room temperature naturally.

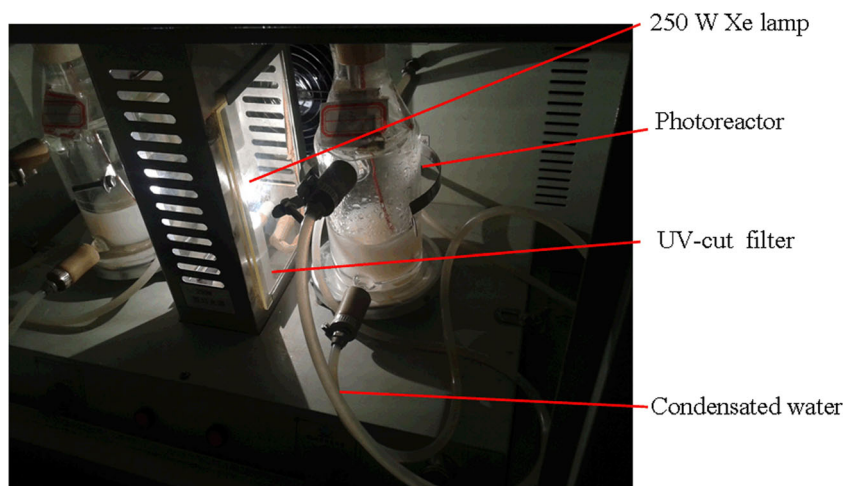
Characterization

All of the products were identified by X-ray diffraction (XRD; Bruker D8 Advance diffractometer, 50 kV, 300 mA) using Cu-Kα radiation. The morphologies and size of the obtained samples were characterized by the transmission electron microscopy (TEM), and the TEM images were visualized on a F20S-TWIN electron microscope (200 kV). The UV-Vis spectra of the products were obtained on a UV-Vis spectrophotometer (UV2450, Shimadzu, Japan), and the BaSO₄ was used as the reference. The high-resolution X-ray photoelectron spectroscopies (XPS; Thermo Escalab 250Xi) were analyzed by a PHI Quantum 2000 XPS system (Al Kα). The photoluminescence spectra (PL) were obtained on a F4500 (Hitachi, Japan) photoluminescence detector, and the Fourier transform infrared spectroscopy (FTIR) was

Table 1 The mass ratio of urea and melamine and symbol

Urea/melamine	10/0	9/1	8/2	7/3	6/4	5/5	4/6	3/7	2/8	1/9	0/10
Symbol	CNU	CN1	CN2	CN3	CN4	CN5	CN6	CN7	CN8	CN9	CNM

Scheme 1 The glass filter of the equipment



characterized on a Nicolet 6700 spectrometer using pressed KBr disks. Raman spectroscopies (Lab-Ram HR Raman spectrometer, JY-Horiba) were excited by a He-Ne laser with wavelength of 780 nm. The ESR (Bruker ECS106 X-band spectrometer) signals of radicals were trapped by spintrap reagent 5, 5-dimethyl-1-pyrroline-N-oxide (DMPO; Sigma Chemical Co.). Total organic carbon (TOC) analyses were conducted on a multi N/C 2100 (Analytik Jena AG, Germany) TOC analyzer.

Photocatalysis evaluation

RhB and TC were used as the model organic pollutant to evaluate the photocatalytic activity of the obtained samples under visible light irradiation, respectively. The photodegradation of RhB and TC were carried out in a photochemical reactor, where the 100 mg sample and 100 mL of 10 mg/L (equal to 10 ppm) RhB or TC solution were contained. To exclude the influence of physical adsorption, the reactor was kept in the dark for 60 min to reach the adsorption equilibrium. Then, a 250-W xenon lamp as the light source was located about 8 cm to one side of the containing solution, which has a glass filter to remove the UV light, like our previous report (Hong et al. 2016), as is shown in Scheme 1.

The photocatalytic degradation ratio of the samples was calculated by the following formula:

$$DR = (1 - A_i / A_0) \times 100\%$$

In this equation, DR is on half of the photocatalytic degradation ratio, A_0 is the initial absorbency of RhB or TC after reached absorption equilibrium, while A_i is the absorbency after the photocatalytic reaction. At each time interval, photocatalysts were

separated by centrifugation at 10,000 rpm for some minutes, and the light absorption of clear solution for the different samples was measured by an UV-Vis spectrophotometer.

Photocatalytic hydrogen productions

The photocatalytic H_2 production was tested using a Lab- H_2 photocatalytic system. A Xe lamp ($\lambda > 400$ nm) was applied as the light source and parallel placed with the reactor. In a typical photocatalytic H_2 production experiment, 0.1 g photocatalyst was dispersed in 200 mL 25% methanol aqueous solution with vigorous stirring and stirred continuously to ensure uniform irradiation of the catalyst suspension during the whole process. Before irradiation, the system was vacuumized to remove the dissolved oxygen in water. The generated gas was collected once an hour, and the amount of hydrogen content was analyzed by gas chromatograph (GC-14C, Shimadzu, Japan, TCD, with argon as a carrier gas).

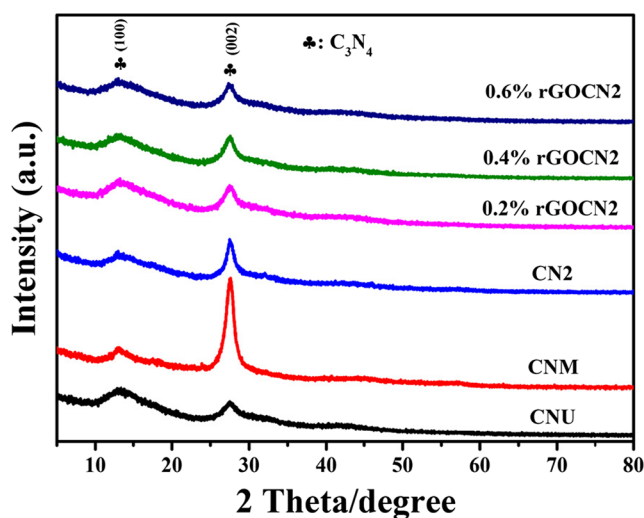
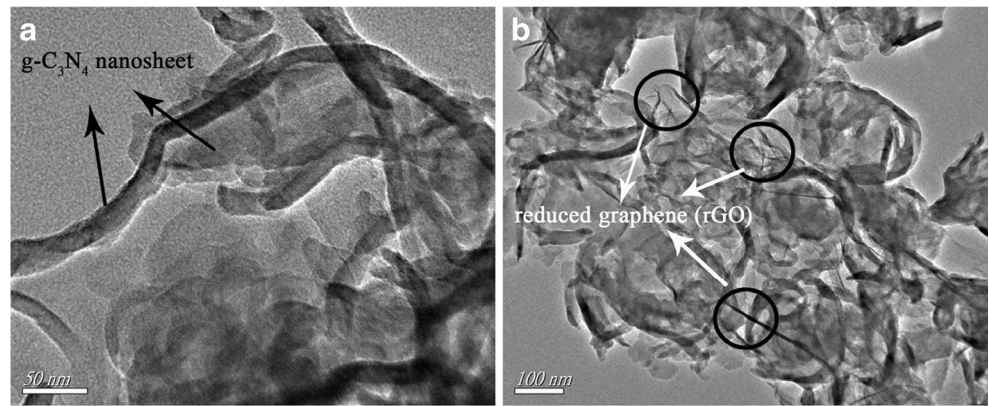


Fig. 1 XRD patterns of CN2, X % rGOCN2 (X = 0.2, 0.4, 0.6) composite photocatalysts

Fig. 2 TEM image CN2 (a) and 0.4% rGO/CN2 (b)



Results and discussion

XRD analysis

In order to determine the crystal structure, the obtained samples were carefully checked by XRD. The CNU, CNM, and the composite patterns were shown in Fig. 1. The strong

interplanar stacking peak of aromatic systems around 14.3 and in-plane repeat units around 27.6° can be observed, corresponding to the (100) and (002) planes of g-C₃N₄, respectively (Wang et al. 2009). And the results confirmed that the g-C₃N₄ was synthesized successfully. In addition, the image shows that the obvious difference of the intensity and the peak intensity of CN2 was located between CNU to CNM. This

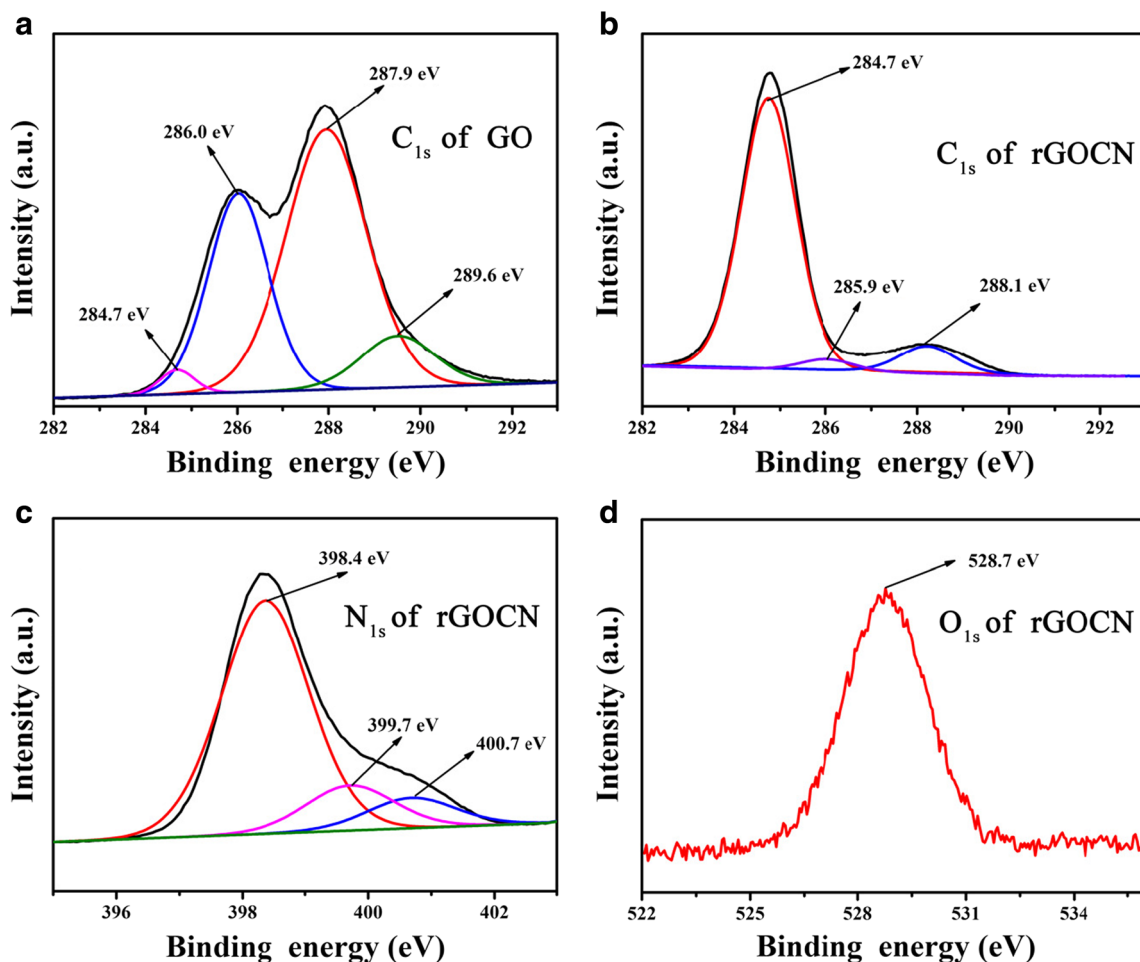


Fig. 3 High-resolution C_{1s} spectrum of GO (a) and 0.4% rGO/CN2 (b). High-resolution N_{1s} spectrum (c). High-resolution O_{1s} spectrum (d)

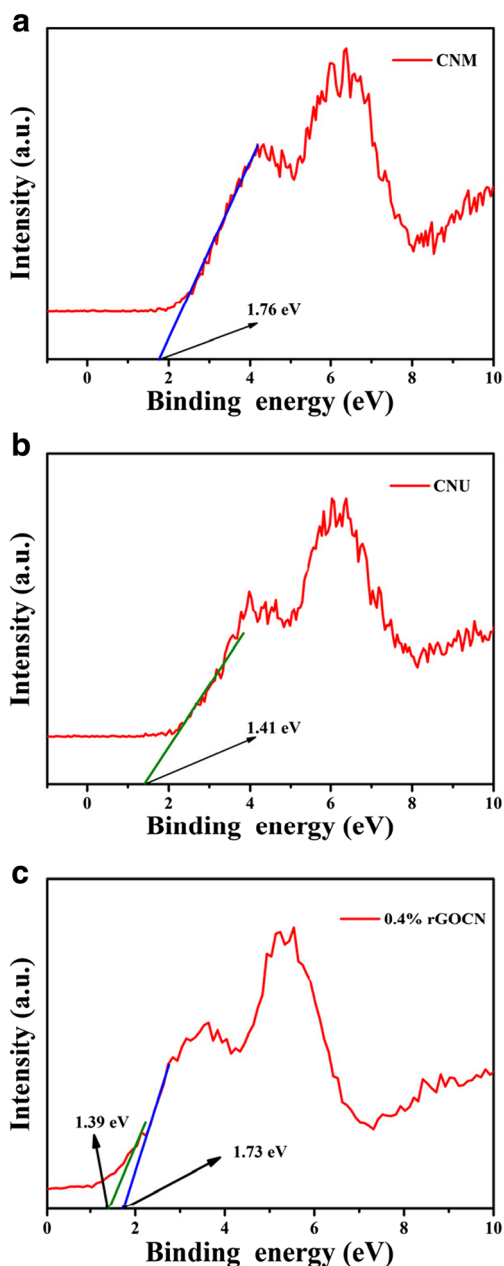


Fig. 4 Valence band XPS spectra of CNM (a), CNU (b), and 0.4% rGO/CN (c)

result indicates that the XRD of the composites was affected by CNU and CNM simultaneously, and the two kinds of material are also contained in the samples at the same time. However, the XRD patterns of X % rGO/CN (X = 0.2, 0.4, 0.6) shows only diffraction features of $g\text{-C}_3\text{N}_4$, as shown in Fig. 1. The reasons for the results mainly because the rGO in those samples were well dispersed in the samples and the contents were quite low (Fan et al. 2015; Lee et al. 2012; Xu et al. 2010). Moreover, there are no significant differences in the intensities and widths of the XRD peaks between X % rGO/CN and the $g\text{-C}_3\text{N}_4$, which demonstrated that the phase

structure and crystallite size of the composites have not been changed after loaded graphene.

Characterization of morphology and structure

The morphology of the obtained samples was viewed by TEM. The TEM image of the CN2 (Fig. 2a) shows that the thicker nanosheets and ultrathin nanosheets are easily found and closely integrated, resulting in the formation of CN2 hybrids. In addition, compared with the agglomerates, the different $g\text{-C}_3\text{N}_4$ in the CN2 composite was well exfoliated into dispersed nanosheets. Thus, the mixture of urea and melamine has a certain inhibition effect on the agglomeration of forming $g\text{-C}_3\text{N}_4$. And the result can be further confirmed by the TEM image of 0.4% rGO/CN2 (Fig. 2b). As can be seen in this figure, CNU and CNM are integrated closely, and the agglomeration of CN is significantly reduced. Moreover, the paper-fold thinner sheet of rGO was found in the image, indicating that the graphene is overlaid on the surface or the interlayers of CN2 composite uniformly. As shown in the image, $g\text{-C}_3\text{N}_4$ and rGO were closely combined, and formed a structure like the sandwich, which will greatly improve the transfer of photogenerated charge, and then improve their photocatalytic activity.

XPS analysis

The high-resolution XPS were carried out to study the surface composition and elemental valence state (Dong et al. 2013a; Dosado et al. 2015; Wang et al. 2014). In order to prove that the graphene oxide sheets have been reduced into rGO during the synthesis process, the C_{1s} spectra of graphene (Fig. 3a) and 0.4% rGO/CN2 (Fig. 3b) were researched. As can be seen from the images, the C_{1s} could be divided into four different peaks at 284.7, 286.0, 287.9, and 289.6 eV, which were assigned to the C–C/C=C, C–OH (hydroxyl), >C=O (carbonyl), and O–C=O (carboxyl) groups, respectively (Chen et al. 2015). The C_{1s} peak intensities at 285.9 and 288.1 eV in 0.4% rGO/CN2 sample revealed obvious decreased, and the peak at 289.6 eV was disappeared compared with that of pristine graphene oxide, which indicates that the oxygen-containing functional groups of hydroxyl, carbonyl, and carboxyl have been removed completely or partially. Thus, this result can explain that the graphene oxide sheets have been reduced again. The high-resolution N_{1s} XPS spectra of 0.4% rGO/CN2 were displayed in Fig. 3c. The binding energy at 398.4 eV could be attributed to Sp^2 hybridized (N–C=N), and the two peaks at 399.7 and 400.7 eV are related to amino functional groups (C–N–H) and tertiary nitrogen groups (N–(C)₃), respectively (Hu et al. 2015; Huang et al. 2015). The high-resolution O_{1s} (527.8 eV; Fig. 3d) can be attributed to the lattice oxygen species of the sample.

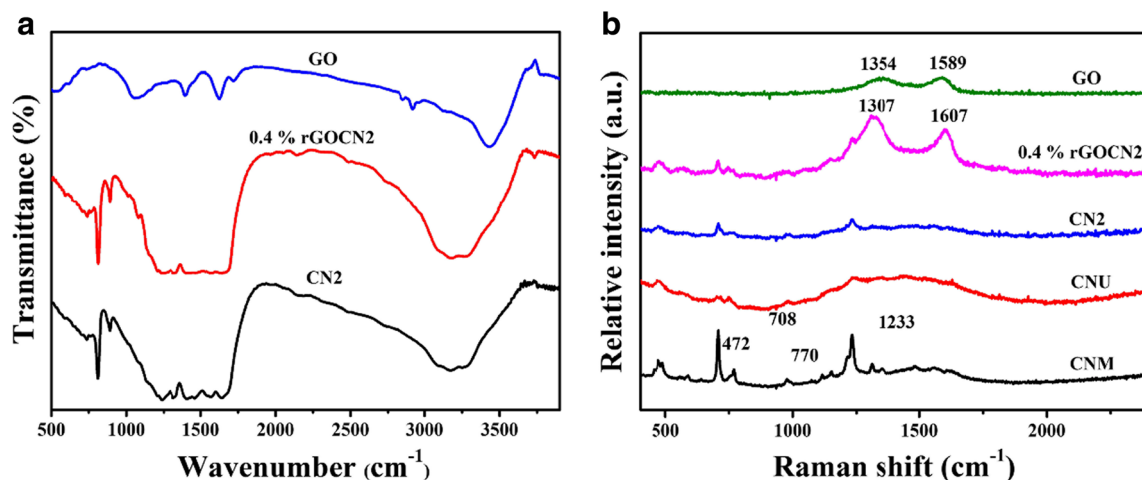


Fig. 5 FTIR spectra (a) and Raman spectra (b) of different samples

Moreover, the valance bands of g-C₃N₄ samples from urea and melamine were examined by VB XPS (Shi et al. 2014). It can be seen that the VB of CNM (1.76 eV; Fig. 4a) was more positive than that of CNU (1.41 eV; Fig. 4b). Synthesizing the above results, the CB position of CNU and CNM can be calculated to be -1.15 and -0.74 eV, respectively. Thus, the VB of CNU is lower than that of CNM, while the CB bottom of CNM is higher than that of CNU. In addition, the VB of 0.4% rGOCN2 sample (Fig. 4c) shows both VB of CNU and CNM, which revealed that the two-phase g-C₃N₄ is also contained in the samples at the same time (Akhavan 2010; Venditti et al. 2015). On the basis of the above results, a band structure scheme for the enhanced photocatalytic activity over the g-C₃N₄ heterojunction can be obtained.

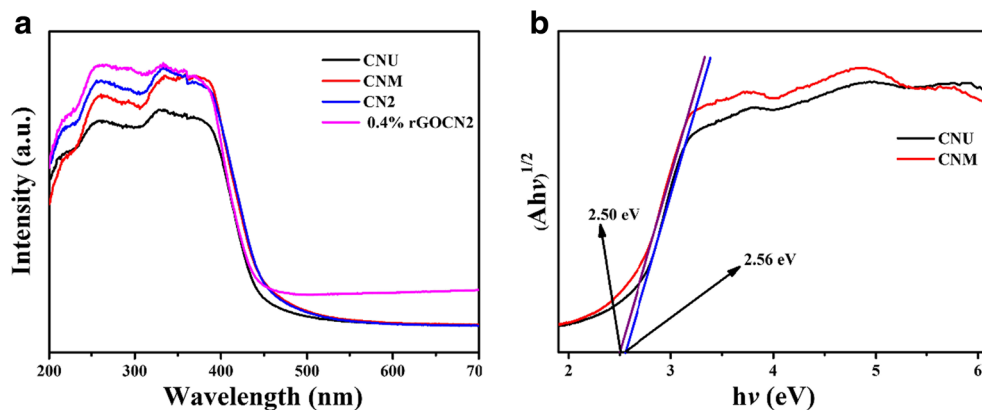
FTIR and Raman spectrum analysis

In order to confirm the molecular structure of the CN and the change of GO, the obtained samples were characterized by FTIR spectra. From the spectra (Fig. 5a), it can be seen that the CN2 photocatalysts own the absorption bands in the region of 810–879 and 1200–1650 cm⁻¹, corresponding to

breathing mode of the triazine units and the typical stretching modes of C–N heterocycles, respectively (Martha et al. 2013; Shalom et al. 2014). Thus, the results reveal that the molecular structure was in accordance with the previous reported in the literature. For the GO, CN2, and the 0.4% rGOCN2 FTIR spectra, the absorptions at about 1049, 1400, 1623, 1718, and 3432 cm⁻¹ can be attributed to the C–O stretching vibrations, C–OH group stretching, C–OH bending vibration, the C = O stretching of COOH groups, and stretching vibration of O–H, respectively (Chen et al. 2015). Compared with the pure graphene, the rGO in CN2 shows obvious different in its spectra. The typical absorption peaks at 1049, 1718, and 3432 cm⁻¹ decrease noticeably in intensity or even disappear. In addition, the peaks at 1400 and 1623 cm⁻¹ were superimposed with g-C₃N₄, which result in the disappearance of the characteristic peak. Thus, the result indicated that the oxygen-containing and functional groups have been removed completely or partially.

Raman analysis was also carried out to further investigate the structure for the prepared samples. As shown in Fig. 5b, four absorption peaks at 472, 708, 770, and 1233 cm⁻¹ are observed in the spectra of CNU and CNM, corresponding to

Fig. 6 a UV-Vis diffuse reflectance spectra of CN2, X % rGOCN2 (X = 0.2, 0.4, 0.6) composite photocatalysts. b The estimated band gap energies of CNM and CNU



the characteristic peaks of g-C₃N₄ (Hou et al. 2013). The intensities of CNU were lower than the CNM obviously, and intensities of CN2 in the middle of the two pure g-C₃N₄, which indicate that the two kinds of material are also contained in the samples at the same time again. Moreover, the pure GO shows that two characteristic peaks at 1354 and 1589 cm⁻¹ can be indexed to the disordered carbon band (D band) and graphite carbon band (G band), corresponding to the first-order zone boundary phonons and the in-plane vibration of Sp² carbon atoms, respectively. Thus, the D band can represent the carbon materials defect degree and the G band can represent the level of Sp² hybridization of graphite. For the 0.4% rGOCN2 composite, all characteristic peak of g-C₃N₄ and graphite can be found in the Raman spectra, which demonstrated that the composite contained g-C₃N₄ and graphite at the same time. In addition, compared with GO, the D band the G band shifts to 1307 and 1586 cm⁻¹ from 1354 and 1589 cm⁻¹, which matches the value of pristine graphite (1586 cm⁻¹), indicating the reduction of graphene-oxide (Xiang et al. 2011).

Optical absorption studies

The optical property of the obtained sample was characterized by UV-Vis diffuse reflectance spectroscopy, as shown in Fig. 6. The different sample shows different absorption edges, which revealed that those samples possess different band gaps. The CNU and CNM exhibit a noticeable difference in its absorption onset at a wavelength of approximately 200–530 nm. As shown in Fig. 6b, the band gap energies of CNU and CNM were estimated as 2.50 and 2.56 eV. Thus, the heterojunction can be formed due to their different band gap energies, valence, and conduction band position of those two g-C₃N₄ semiconductors, and this conclusion will be further demonstrated below. However, once the junction was formed, the composites will show different absorbance with different proportions of urea and melamine. In addition, the pure g-C₃N₄ shows a quite similar absorption onset at 530–700 nm. With loading the GO into the CN2 composite, the 0.4% rGOCN2 samples showed an enhanced absorption at UV region and quite obvious enhancement in the long-wavelength region.

Photocatalytic degradation of organic pollutants

The photocatalytic activities for photocatalytic degradation of organic pollutants of all the samples were evaluated by photocatalytic degradation of rhodamine B (RhB) and tetracycline under visible light irradiation. Table 2 shows the photocatalytic degradation efficiency for all of the composites samples. The CNU and CNM show the photocatalytic degradation efficiencies of 92.9 and

Table 2 The photocatalytic degradation rates (%) of RhB and TC by different samples

	t (min)	CNU (%)	CN1 (%)	CN3 (%)	CN4 (%)	CN5 (%)	CN6 (%)	CN7 (%)	CN8 (%)	CN9 (%)	CNM (%)	rGOCNU (%)	rGOCNM (%)
RhB	20	43.9	72.2	25.2	27.7	14.3	32.3	35.2	25.6	28	32.7	72.6	63.8
	40	73.4	97.3	59.3	51.9	38.6	62.7	64.5	52.3	51.3	48.5	96.1	90.6
	60	92.9	98.8	98.4	84.9	54.1	87.5	88.9	73.8	74.5	83.3	98.2	97.4
TC	20	23.7	32.5	31.6	26.3	10.2	9.2	12.2	10.9	8.7	27.6	34.8	43.2
	40	49	52.3	58.2	44.7	21.7	19.6	24.4	21.8	18	46.4	77.3	65.4
	60	62	64.5	73.2	59.1	31.5	30.1	35.9	33	28.6	51.9	89.5	73.7

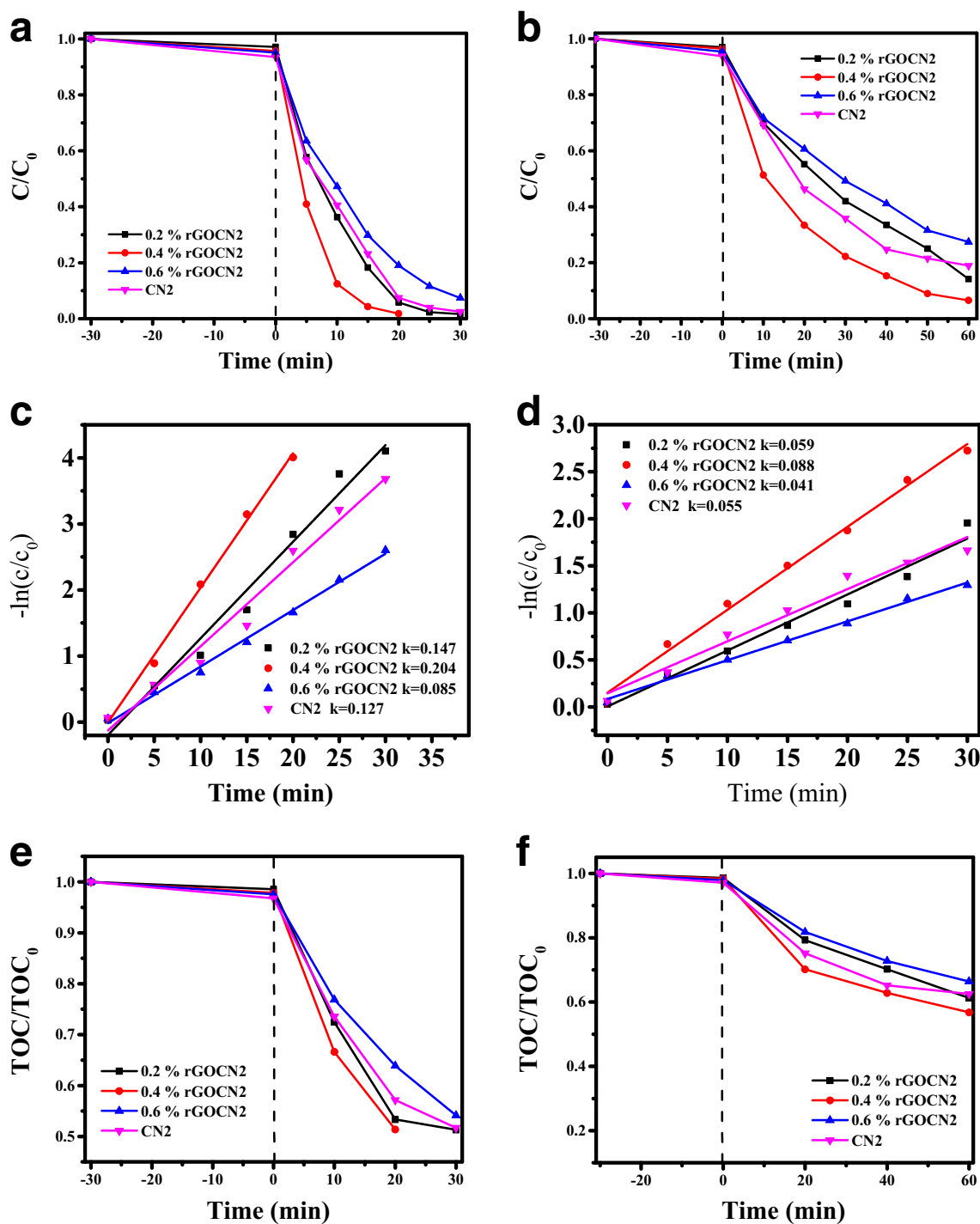


Fig. 7 Photocatalytic degradation of RhB (a) and TC (b) using CN2, X % rGOCN2 (X = 0.2, 0.4, 0.6) composite photocatalysts; the pseudo-first-order reaction kinetics of RhB (c) and TC (d); and the TOC experiments of RhB (e) and TC (f)

83.3% for RhB in 60 min, respectively. However, the degradation effect was obviously improved, when CNU and CNM were integrated in a certain proportion. And, there exists an optimum ratio (urea:melamine = 8:2, CN2) of precursor, which exhibits a best photocatalytic degradation efficiency of 97.3% in 30 min. Similar to the results of RhB, the CNU and CNM show lower

photocatalytic degradation efficiencies of 62.0 and 51.9% for the tetracycline, and the optimum samples of CN2 can get the best degradation efficiency of 80.0% in 60 min. Figure 7 presents a comparison of the degradation efficiency of the CN2, and X% rGOCN2 (X = 0.2, 0.4, 0.6) samples. As can be seen in this figure, the photocatalytic activity of the samples has a significant influence

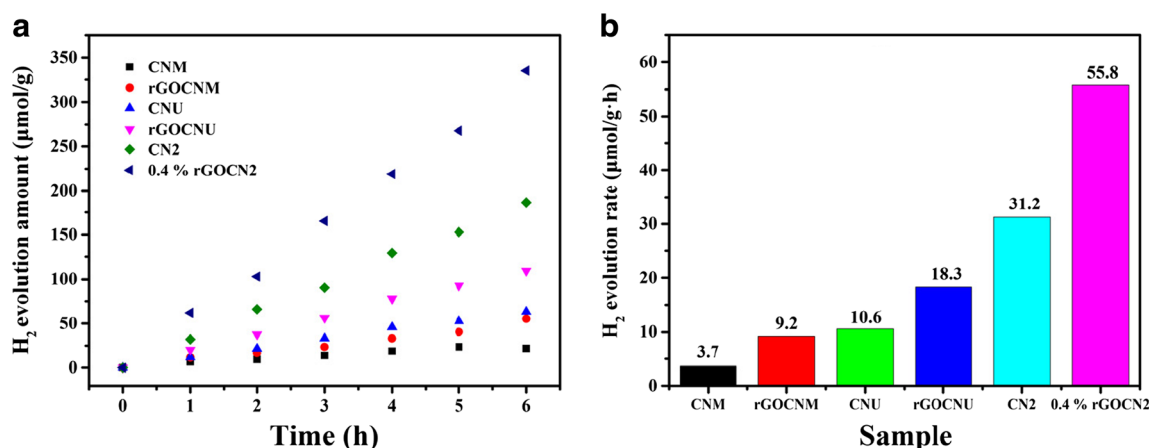


Fig. 8 Plots of photocatalytic H₂ evolution amount (a) and comparison of the H₂ evolution rate (b) in the absence of the cocatalyst for different samples

by the graphene content. Compared with the CN2, the 0.4% rGOCN2 sample exhibits an obvious enhancement for the photocatalytic activity under the visible light irradiation. With the rGO contents increasing, the photocatalytic activity was obviously improved, and the highest degradation rate was obtained when the contents of graphene increase to 0.4%. For this sample, the RhB can be degraded completely in 20 min (Fig. 7a), and degradation efficiency can be reached to 93.2% for the tetracycline in 60 min (Fig. 7b). And the absorbency of the samples is low, smaller than 5%. In addition, the 0.4% rGOCN2 composite shows high photocatalytic activity than rGOCNU and rGOCNM samples. However, the photocatalytic activity was decreased with further increasing the contents of GO for the CN2 photocatalyst sample. The possible reason is that the superfluous GO will be covered on the surface of CN2 and then reduce the numbers of CN2 active sites available for photocatalytic reaction. Figure 7c, d shows that the photocatalytic degradation of RhB and tetracycline by the obtained samples fits the pseudo-first-order kinetics, $\ln(C/C_0) = kt$, where K , C , and C_0 are the apparent reaction rate constant, the concentration at time t , and the initial concentration of the contaminant, respectively. As can be seen from the two figures, the time and $-\ln(C/C_0)$ shows an obviously linear relationship, which revealed the above degradation experimental results again. The total organic carbon (TOC)

removal rates of the samples for degradation of RhB and TC are shown in Fig. 7e, f. It can be observed that the best removal of TOC was reached 0.487 and 0.433 after photoreaction, indicating that the RhB and TC can be good mineralized.

Photocatalytic hydrogen productions

To further investigate the performance of the samples, we have executed hydrogen evolution experiments. As shown in Fig. 8a, b, in the absence of cocatalyst, the CNM and CNU show lower H₂ evolution rate of 3.7 and 10.6 μmol/g h, respectively. Even after loading of graphene, the hydrogen production rate can only reach 9.2 and 18.3 μmol/g h for CNM and CNU, respectively. However, the CN2 showed obviously enhanced photocatalytic activity (31.2 μmol/g h) as compared with pure g-C₃N₄, which was caused by the formed junction between two phases of g-C₃N₄. In addition, the H₂ evolution rate will be further increased with loading graphene, because of the graphene can transfer to the interfacial photogenerated charge carriers efficiently so that it can suppress charge recombination and enhance photocatalytic activity efficiently. The results indicated that the H₂ evolution rate has a gap compared with the Pt/samples. Fortunately, the CN2 and 0.4% rGOCN2 samples, especially the 0.4% rGOCN2 sample, still have a higher H₂ evolution rate,

Table 3 The photocatalytic activity of other similar work

Catalyst	Year	Irradiation	H ₂ evolution rate (μmol/g h)	Ref
C ₃ N ₄ -MU	2013	Vis (125 W)	10	Martha et al. (2013)
M-g-C ₃ N ₄	2017	UV (150 W)	780.5	Zhou et al. (2017)
Pt-rGO/g-C ₃ N ₄ (0.08%)	2017	LED (300 W)	874	Sun et al. (2016)
0.4% rGOCN2	–	Vis (350 W)	55.8	Our work

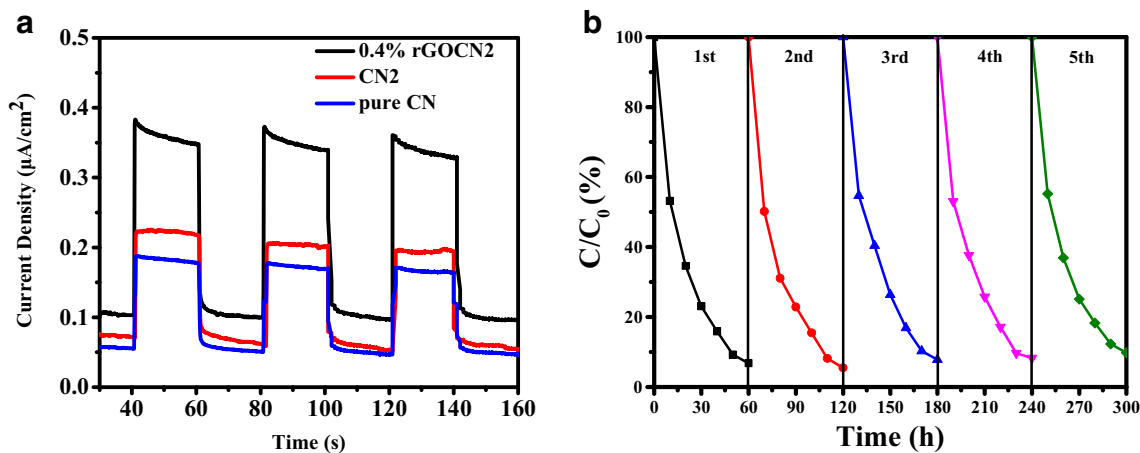


Fig. 9 a The photocurrent spectra of the samples. b Stability experiment for TC removal by 0.4% rGOCN2

and besides, it has avoided using the high cost of precious metals and increased the stability of the photocatalyst (Chang et al. 2014). As is shown in Table 3, the photocatalytic activity of other similar works is compared to our work. It is obvious that the activity of 0.4% rGOCN2 is prior to the same work as Martha’s work. The M-g-C₃N₄ and Pt-rGO/g-C₃N₄ (0.08%) reveal the higher activity, but they are induced by the UV light and LED light.

As is shown in Fig. 9a, the photocurrent of 0.4% rGOCN2 is larger than that of CN2 and pure g-C₃N₄. It indicates that the separation efficiency of photoinduced carriers have been improved a lot by the loaded rGO. The stability of photocatalyst is very important for environmental application, since it can promote significant reduction of the operational cost in photocatalytic process, thus making the application of photocatalysis in TC removal to be foreseeable. After five recycling runs, there is no obvious change in the photocatalytic degradation efficiencies of TC by 0.4% rGOCN2, as is shown in Fig. 9b.

ESR studies

The experiment results were further confirmed by ESR. As can be seen in the Fig. 10, the ESR spectra were measured for the pure g-C₃N₄, CN2, and 0.4% rGOCN2 samples. The result revealed that the 0.4% rGOCN2 samples possess the higher intensity of the characteristic peaks of superoxide radicals than the g-C₃N₄ and CN2 sample, which indicated that this sample was favorable for the formation of higher redox (Hu et al. 2015). Furthermore, the ESR signal of the DMPO-•O₂⁻ is higher than that of DMPO-OH•, as is shown in Fig. 10b. It indicates that the main oxide active species is •O₂⁻.

Photocatalytic degradation mechanisms

A tentative mechanism for the enhanced photocatalytic activity of the 0.4% rGOCN2 sample was illustrated in Scheme 2. Under the irradiation of visible light, the CNU will be excited firstly to produce photogenerated electrons in the CB and

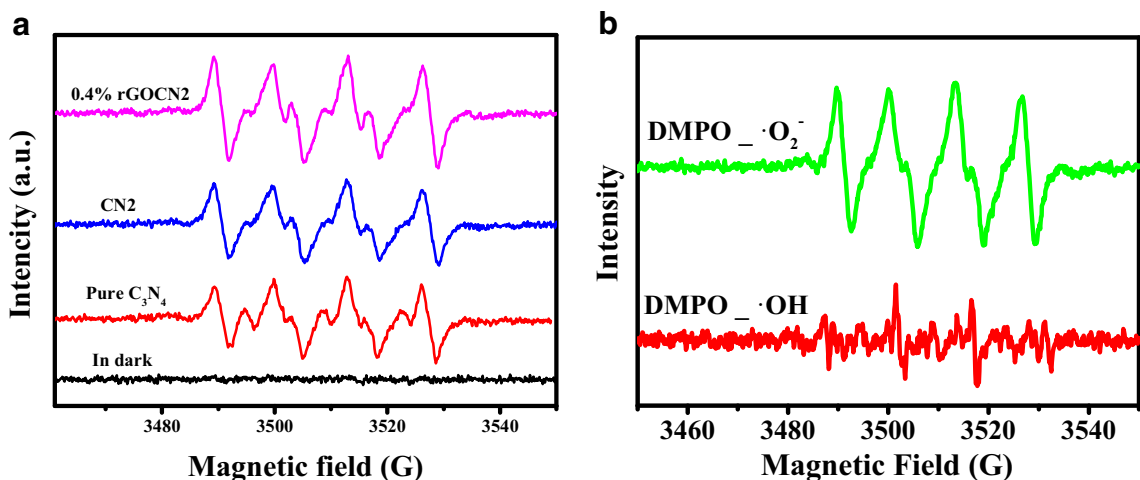
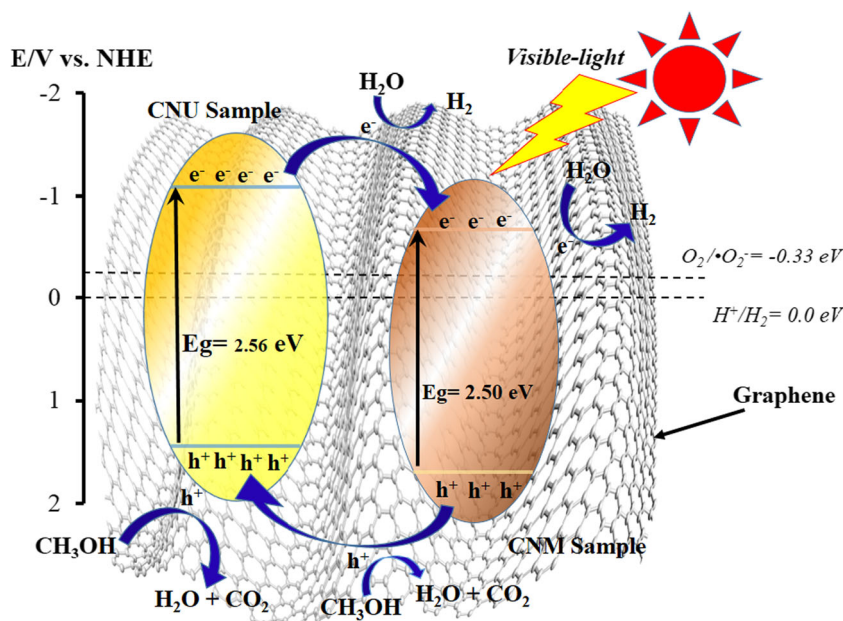


Fig. 10 a Electron spin resonance for different samples. b ESR signals of the DMPO-•O₂⁻ and DMPO-OH•

Scheme 2 Schematic illustrations of the charge transfer in CNO composites



transferred to the surface of CNU photocatalysts because its CB was negative than CNM (Liu et al. 2017). And then, the electrons can transfer to the CB of CNM driven by the different band potential and the photogenerated holes will be transferred to the VB of CNU from the VB of CNM at the same time, resulting in the aggregation of electrons in the CB of CNM and photoexcited holes in the VB of CNU (Akhavan 2015; Wu et al. 2016; Yuan et al. 2018). In addition, the rGO will accelerate the mutual transfer of photogenerated carrier. The aggregation of electrons and holes can be speed up transferred by the rGO to the solution and then participate in the reaction (Chang et al. 2014). Finally, the accumulated electrons on the rGO can be involved in the photochemical reduction of water to generate hydrogen. Simultaneously, the holes in the VB of $g\text{-C}_3\text{N}_4$ are trapped by the methanol as scavengers.

Conclusions

In this work, the two-phase $g\text{-C}_3\text{N}_4$ heterojunctions were synthesized by the precursor of urea and melamine with different proportions, and an optimum ratio of the precursor was funded. As a result, the sample of 0.4% rGO/two-phase $g\text{-C}_3\text{N}_4$ heterojunction photocatalysts can degrade the rhodamine B and tetracycline high efficiently, and it can improve the photocatalytic activity of H_2 evolution from water-splitting under the visible light irradiation. In addition, the rGO acting as electronic conductive channels in the composites can transfer the interfacial photogenerated charge carriers efficiently so that it has suppressed the charge recombination and enhanced the photocatalytic activity. Moreover,

the samples still have a higher H_2 evolution rate in the absence of cocatalyst. The 0.4% rGO loaded samples, 0.4% rGOCN2, own the best performance. Its rate of H_2 evolution was 15 times as high as that of the pure $g\text{-C}_3\text{N}_4$.

Acknowledgments We gratefully acknowledge the financial support of the National Natural Science Foundation of China (21477050), Excellent Youth Foundation of Jiangsu Scientific Committee (BK20140011), Chinese-German Cooperation Research Project (GZ1091), Program for High-Level Innovative and Entrepreneurial Talents in Jiangsu Province, Program for New Century Excellent Talents in University (NCET-13-0835), Henry Fok Education Foundation (141068), and Six Talents Peak Project in Jiangsu Province (XCL-025).

References

- Akhavan O (2010) Graphene nanomesh by ZnO nanorod photocatalysts. *ACS Nano* 4:4174–4180
- Akhavan O (2015) Bacteriorhodopsin as a superior substitute for hydrazine in chemical reduction of single-layer graphene oxide sheets. *Carbon* 81:158–166
- Cao SW, Yu JG (2014) $g\text{-C}_3\text{N}_4$ -based photocatalysts for hydrogen generation. *J Phys Chem Lett* 5:2101–2107
- Chang K, Mei ZW, Wang T, Kang Q, Ouyang SX, Ye JH (2014) MoS_2 /graphene cocatalyst for efficient photocatalytic H_2 evolution under visible light irradiation. *ACS Nano* 8:7078–7087
- Chen J, Shen SH, Guo PH, Wang M, Wu P, Wang XX, Guo LJ (2014) In-situ reduction synthesis of nano-sized Cu_2O particles modifying $g\text{-C}_3\text{N}_4$ for enhanced photocatalytic hydrogen production. *Appl Catal B Environ*. 152:335–341
- Chen W, Duan GR, Liu TY, Chen SM, Liu XH (2015) Fabrication of Bi_2MoO_6 nanoplates hybridized with $g\text{-C}_3\text{N}_4$ nanosheets as highly efficient visible light responsive heterojunction photocatalysts for rhodamine B degradation. *Mater Sci Semicond Process* 35:45–54
- Dong F, Wang ZY, Sun YJ, Ho WK, Zhang HD (2013a) Engineering the nanoarchitecture and texture of polymeric carbon nitride

- semiconductor for enhanced visible light photocatalytic activity. *J Colloid Interface Sci* 401:70–79
- Dong F, Zhao ZW, Xiong T, Ni ZL, Zhang WD, Sun YJ, Ho WK (2013b) In situ construction of g-C₃N₄/g-C₃N₄ metal-free heterojunction for enhanced visible-light photocatalysis. *ACS Appl Mater Interfaces* 5:11392–11401
- Dosado AG, Chen WT, Chan A, Sun-Waterhouse D, Waterhouse GIN (2015) Novel au/TiO₂ photocatalysts for hydrogen production in alcohol-water mixtures based on hydrogen titanate nanotube precursors. *J Catal* 330:238–254
- Fan MS, Hu B, Yan X, Song CJ, Chen TJ, Feng Y, Shi WD (2015) Excellent visible-light-driven photocatalytic performance of Cu₂O sensitized NaNbO₃ heterostructures. *New J Chem* 39:6171–6177
- Hong JD, Xia XY, Wang YS, Xu R (2012) Mesoporous carbon nitride with in situ sulfur doping for enhanced photocatalytic hydrogen evolution from water under visible light. *J Mater Chem* 22:15006–15012
- Hong YZ, Li CS, Zhang GY, Meng YD, Yin BX, Zhao Y, Shi WD (2016) Efficient and stable Nb₂O₅ modified g-C₃N₄ photocatalyst for removal of antibiotic pollutant. *Chem Eng J* 299:74–84
- Hou JG, Yang C, Cheng HJ, Jiao SQ, Takeda O, Zhu HM (2014) High-performance p-Cu₂O/n-TaON heterojunction nanorod photoanodes passivated with an ultrathin carbon sheath for photoelectrochemical water splitting. *Energy Environ Sci* 7:3758–3768
- Hou Y, Wen ZH, Cui SM, Guo XR, Chen JH (2013) Constructing 2D porous graphitic C₃N₄ nanosheets/nitrogen-doped graphene/layered MoS₂ ternary nanojunction with enhanced photoelectrochemical activity. *Adv Mater* 25:6291–6297
- Hu B, Cai FP, Chen TJ, Fan MS, Song CJ, Yan X, Shi WD (2015) Hydrothermal synthesis g-C₃N₄/Nano-InVO₄ nanocomposites and enhanced photocatalytic activity for hydrogen production under visible light irradiation. *ACS Appl Mater Interfaces* 7:18247–18256
- Huang LY, Xu H, Li YP, Li HM, Cheng XN, Xia JX, Xu YG, Cai GB (2013) Visible-light-induced WO₃/g-C₃N₄ composites with enhanced photocatalytic activity. *Dalton Trans* 42:8606–8616
- Huang ZA, Sun Q, Lv KL, Zhang ZH, Li M, Li B (2015) Effect of contact interface between TiO₂ and g-C₃N₄ on the photoreactivity of g-C₃N₄/TiO₂ photocatalyst: (001) vs (101) facets of TiO₂. *Appl. Catal. B Environ.* 164:420–427
- Hurum DC, Agrios AG, Gray KA, Rajh T, Thurnauer MC (2003) Explaining the enhanced photocatalytic activity of Degussa P25 mixed-phase TiO₂ using EPR. *J Phys Chem B* 107:4545–4549
- Lee JS, You KH, Park CB (2012) Highly photoactive, low bandgap TiO₂ nanoparticles wrapped by graphene. *Adv Mater* 24:1084–1088
- Liau LCK, Lin YC, Peng YJ (2013) Fabrication pathways of p-n Cu₂O homojunction films by electrochemical deposition processing. *J Phys Chem C* 117:26426–26431
- Liu LQ, Zhang XN, Yang LF, Ren LT, Wang DF, Ye JH (2017) Metal nanoparticles induced photocatalysis. *Nat. Sci. Rev.* 4:761–780
- Martha S, Nashim A, Parida KM (2013) Facile synthesis of highly active g-C₃N₄ for efficient hydrogen production under visible light. *J Mater Chem A* 1:7816–7824
- Shalom M, Guttentag M, Fettekenhauer C, Inal S, Neher D, Llobet A, Antonietti M (2014) In situ formation of heterojunctions in modified graphitic carbon nitride: synthesis and noble metal free photocatalysis. *Chem. Mater.* 26:5812–5818
- Shi HF, Chen GQ, Zhang CL, Zou ZG (2014) Polymeric g-C₃N₄ coupled with NaNbO₃ nanowires toward enhanced photocatalytic reduction of CO₂ into renewable fuel. *ACS Catal* 4:3637–3643
- Shown I, Hsu HC, Chang YC, Lin CH, Roy PK, Ganguly A, Wang CH, Chang JK, Wu CI, Chen LC, Chen KH (2014) Highly efficient visible light photocatalytic reduction of CO₂ to hydrocarbon fuels by carbon nanoparticle decorated graphene oxide. *Nano Lett* 14:6097–6103
- Song CJ, Fan MS, Hu B, Chen TJ, Wang LP, Shi WD (2015) Synthesis of a g-C₃N₄-sensitized and NaNbO₃-substrated II-type heterojunction with enhanced photocatalytic degradation activity. *CrystEngComm* 17:4575–4583
- Su CL, Acik M, Takai K, Lu J, Hao SJ, Zheng Y, Wu PP, Bao QL, Enoki T, Chabal YJ, Loh KP (2012) Probing the catalytic activity of porous graphene oxide and the origin of this behaviour. *Nat Commun* 3:9
- Sun B, Vorontsov AV, Smirniotis PG (2003) Role of platinum deposited on TiO₂ in phenol photocatalytic oxidation. *Langmuir* 19:3151–3156
- Sun JX, Yuan YP, Qiu LG, Jiang X, Xie AJ, Shen YH, Zhu JF (2012) Fabrication of composite photocatalyst g-C₃N₄-ZnO and enhancement of photocatalytic activity under visible light. *Dalton Trans* 41: 6756–6763
- Sun Q, Wang P, Yu HG, Wang XF (2016) In situ hydrothermal synthesis and enhanced photocatalytic H₂-evolution performance of suspended rGO/g-C₃N₄ photocatalysts. *J. Mol. Catal. A Chem.* 424:369–376
- Venditti I, Hassanein TF, Fratoddi I, Fontana L, Battocchio C, Rinaldi F, Carafa M, Marianecci C, Diociaiuti M, Agostinelli E, Cametti C, Russo MV (2015) Bioconjugation of gold-polymer core-shell nanoparticles with bovine serum amine oxidase for biomedical applications. *Colloids Surf. B Biointerfaces* 134:314–321
- Walter MG, Warren EL, McKone JR, Boettcher SW, Mi QX, Santori EA, Lewis NS (2010) Solar water splitting cells. *Chem Rev* 110:6446–6473
- Wang P, Chen P, Kostka A, Marschall R, Wark M (2013) Control of phase coexistence in calcium tantalate composite photocatalysts for highly efficient hydrogen production. *Chem. Mater.* 25:4739–4745
- Wang T, Meng XG, Li P, Ouyang SX, Chang K, Liu GG, Mei ZW, Ye JH (2014) Photoreduction of CO₂ over the well-crystallized ordered mesoporous TiO₂ with the confined space effect. *Nano Energy* 9:50–60
- Wang X, Xu Q, Li MR, Shen S, Wang XL, Wang YC, Feng ZC, Shi JY, Han HX, Li C (2012) Photocatalytic overall water splitting promoted by an alpha-beta phase junction on Ga₂O₃. *Angew. Chem. Int. Ed.* 51:13089–13092
- Wang XC, Maeda K, Thomas A, Takanabe K, Xin G, Carlsson JM, Domen K, Antonietti M (2009) A metal-free polymeric photocatalyst for hydrogen production from water under visible light. *Nat Mater* 8:76–80
- Wu LC, Zhao H, Jin LG, Xu HY (2016) TiO₂/g-C₃N₄ heterojunctions: in situ fabrication mechanism and enhanced photocatalytic activity. *Front Mater Sci* 10:310–319
- Xiang QJ, Yu JG, Jaroniec M (2011) Preparation and enhanced visible-light photocatalytic H₂-production activity of graphene/C₃N₄ composites. *J Phys Chem C* 115:7355–7363
- Xiang QJ, Yu JG, Jaroniec M (2012) Graphene-based semiconductor photocatalysts. *Chem Soc Rev* 41:782–796
- Xu HY, Liu WC, Shi J, Zhao H, Qi SY (2014) Photocatalytic discoloration of methyl Orange by anatase/schorl composite: optimization using response surface method. *Environ Sci Pollut Res* 21:1582–1591
- Xu HY, Shi TN, Zhao H, Jin LG, Wang FC, Wang CY, Qi SY (2016a) Heterogeneous Fenton-like discoloration of methyl orange using Fe₃O₄/MWCNTs as catalyst: process optimization by response surface methodology. *Front Mater Sci* 10:45–55
- Xu HY, Wu LC, Jin LG, Wu KJ (2017a) Combination mechanism and enhanced visible-light photocatalytic activity and stability of CdS/g-C₃N₄ heterojunctions. *J. Mater. Sci. Technol.* 33:30–38
- Xu J, Wu HT, Wang X, Xue B, Li YX, Cao Y (2013) A new and environmentally benign precursor for the synthesis of mesoporous g-C₃N₄ with tunable surface area. *Phys Chem Chem Phys* 15:4510–4517
- Xu WJ, Liu XH, Ren JW, Zhang P, Wang YQ, Guo YL, Guo Y, Lu GZ (2010) A novel mesoporous Pd/cobalt aluminate bifunctional catalyst for aldol condensation and following hydrogenation. *Catal Commun* 11:721–726
- Xu ZH, Zhang DF, Chen WF, Li YR, Yuan SJ (2016b) Nanoscale iron oxides loaded granular activated carbon (GAC-NSIO) for cadmium removal. *Desalin Water Treat* 57:3559–3571
- Xu ZH, Zhang DF, Yuan ZH, Chen WF, Zhang TQ, Tian DQ, Deng HX (2017b) Physicochemical and adsorptive characteristics of activated carbons from waste polyester textiles utilizing MgO template method. *Environ Sci Pollut Res* 24:22602–22612

- Yan SC, Lv SB, Li ZS, Zou ZG (2010) Organic-inorganic composite photocatalyst of g-C₃N₄ and TaON with improved visible light photocatalytic activities. *Dalton Trans* 39:1488–1491
- Yan X, Wang XY, Gu W, Wu MM, Yan Y, Hu B, Che GB, Han DL, Yang JH, Fan W, Shi WD (2015) Single-crystalline AgIn(MoO₄)₂ nanosheets grafted ag/AgBr composites with enhanced plasmonic photocatalytic activity for degradation of tetracycline under visible light. *Appl. Catal. B-Environ.* 164:297–304
- Yuan YP, Ruan LW, Barber J, Loo SCJ, Xue C (2014) Hetero-nanostructured suspended photocatalysts for solar-to-fuel conversion. *Energy Environ Sci* 7:3934–3951
- Yuan ZH, Xu ZH, Zhang DF, Chen WF, Zhang TQ, Huang YX, Gu L, Deng HX, Tian DQ (2018) Box-Behnken design approach towards optimization of activated carbon synthesized by co-pyrolysis of waste polyester textiles and MgCl₂. *Appl Surf Sci* 427:340–348
- Zhang JS, Zhang MW, Lin S, Fu XZ, Wang XC (2014) Molecular doping of carbon nitride photocatalysts with tunable bandgap and enhanced activity. *J Catal* 310:24–30
- Zhao ZW, Sun YJ, Dong F (2015) Graphitic carbon nitride based nanocomposites: a review. *Nano* 7:15–37
- Zhou MJ, Hou ZH, Zhang L, Liu Y, Gao QZ, Chen XB (2017) N/n junctioned g-C₃N₄ for enhanced photocatalytic H₂ generation. *Sustain. Energy Fuels* 1:317–323